

## Aeroacoustic sources generated by flow–sound interaction in a T-junction



Eric Salt, Saber Mohamed, David Arthurs, Samir Ziada\*

Department of Mechanical Engineering, McMaster University, Hamilton, ON, Canada L8S 4L7

### ARTICLE INFO

**Article history:**

Received 21 September 2013

Accepted 24 August 2014

Available online 26 September 2014

**Keywords:**

Flow-excited acoustic resonance

Flow–sound interaction

T-junction

Side-branch

Aeroacoustic sources

Shear layer

### ABSTRACT

This paper experimentally investigates the flow–sound interaction mechanisms in a T-junction combining the flow from its two co-axial side-branches into the central branch. The T-junction has a sudden area expansion at each side-branch entrance. Flow separation at these area expansions forms free shear layers which are shown to excite the acoustic mode(s) of the branches over several ranges of flow velocity, each of which results from the coupling of the acoustic mode with a different shear layer oscillation mode. Phase-locked particle image velocimetry is utilized to detail the unsteady flow field over the acoustic cycle for two shear layer oscillation modes. Finite element analysis is used to characterize the excited acoustic mode shape and its associated particle velocity field. In-depth analysis of the flow–sound interaction mechanism inside the T-junction is performed by means of Howe's acoustic analogy. It is concluded that the flow–sound interaction mechanism in *the entrance region of the T-junction* produces a spatially alternating pattern of acoustic energy generation and absorption. This alternating pattern of energy exchange between the flow and sound fields results in a minimal amount of net acoustic power being generated in *the entrance region*. However, the increasing orthogonality between the acoustic particle streamlines and the flow streamlines near the *exit of the T-junction at its center* results in the majority of the generated sound power which sustains the acoustic resonance.

© 2014 Elsevier Ltd. All rights reserved.

## 1. Introduction

Piping systems with unique geometries are known to be susceptible to flow-acoustic coupling, resulting in the production of strong acoustic resonances. In particular, T-junctions located within piping networks are especially liable to this phenomenon. Separated shear layers are formed in regions where there are sudden expansions or changes in the flow direction. Due to the inherent instability of these shear layers, small vortices may form and convect with the flow at a frequency defined by the local geometry and flow parameters. As the vortex shedding frequency approaches that of an acoustic resonant mode of a nearby portion of the piping system, flow-acoustic coupling may be initiated. This coupling mechanism starts with the growth of small vorticity perturbations in the separated shear layer. As these growing vorticity perturbations convect through the T-junction, they interact with the acoustic field and create an energy exchange between the flow field and the acoustic field, effectively enhancing or dampening the acoustic response produced by the piping system (Howe, 1980, 1998; Tonon et al., 2011; Ziada and Lafon, 2014). In many cases, flow-excited acoustic resonances can

\* Corresponding author.

E-mail address: [ziadas@mcmaster.ca](mailto:ziadas@mcmaster.ca) (S. Ziada).

develop strong flow-induced vibrations and piercing noise levels. The vibration can cause violent pipe oscillations resulting in fatigue failure, while the acoustic tones can create an environment which is dangerous for plant workers and neighboring communities. Flow induced vibrations of piping systems, as well as the mechanism of sound generation has received much attention in the literature (e.g. Coffman and Bernstein, 1980; Bruggeman et al., 1989, 1991; Koo and Park, 1998; Fagerlund et al., 2005; Ziada, 2010; Tonon et al., 2011; Ziada and Lafon, 2014).

Most of the previous work performed on flow-acoustic coupling in piping systems has been devoted to closed side-branches (e.g. Rockwell and Naudascher, 1978; Bruggeman et al., 1989; Ziada and Bühlmann, 1992; Ziada, 1994; Dequand et al., 2003; and many others). Recently, Tonon et al. (2011) and Ziada and Lafon (2014) published comprehensive reviews of the state of knowledge in this field and Ziada (2010) reported recent industrial case histories related to flow-excited acoustic resonances in closed side-branches. Even though in many respects the sound generation mechanism associated with flow over closed side-branches is comparable to that experienced inside T-junctions with various flow patterns, the flow-acoustic coupling mechanism in T-junctions with merging flows has received little attention. Karlsson and Åbom (2010) conducted a study of the aeroacoustic properties of side-branch orifices. Ziada et al. (2007) investigated the aeroacoustic response of a variety of standard T-junction geometries and concluded that the most liable acoustic modes for excitation are those extending along the side-branches with a pressure node located at the T-junction. Furthermore, they also reported that very little noise is produced by T-junction geometries without a transition region, created by a flow area expansion at the T-junction inlet sections, as illustrated by the inset in Fig. 1. This flow geometry appears to have some similarities with the whistling nozzle, which consists of a short piece of sudden pipe expansion at the nozzle exit (Hirschberg et al., 1989; van Lier et al., 2001), but it is actually more complex as it involves the impingement of two opposing flows followed by a change of 90° in the direction of the merging flows. In a related paper, Ziada et al. (2009) conducted a qualitative flow visualization study of a T-junction using a phase locked strobe light and smoke injectors. They proposed that most of the sound power production can be attributed to flow separation in the transition region along the outer wall of the T-junction (see Fig. 1). In addition, half the length of the T-junction transition section, length  $L_c$  in Fig. 1, was found to be the characteristic length scale controlling the reduced velocity over which acoustic resonances are excited. Although these studies provided valuable information about the ranges of flow and geometric parameters at which acoustic resonances may be excited, the details of the excitation mechanism and the nature of the aeroacoustic sources causing the resonance remain largely unexplored.

The objective of the current study is to further understand the flow-acoustic coupling mechanism present in a T-junction and explore the spatial characteristics of the resulting aeroacoustic sources. To achieve this, the details of the unsteady flow field in the T-junction will be defined quantitatively by means of particle imaging velocimetry and the sound field of the excited acoustic mode is computed numerically. The flow field and acoustic field can then be combined to find details of the acoustic power generation using, what is referred to in this paper as, Howe's Theorem

$$\Omega = -\rho \int (\mathbf{v} \times \mathbf{u}_{ac}) \omega \, dV, \quad (1)$$

where  $\rho$  is the density of the fluid convecting at a velocity,  $\mathbf{v}$ , and vorticity,  $\omega$ , while  $\mathbf{u}_{ac}$  is the acoustic particle velocity of the sound field. As the equation is integrated over the volume of the T-junction,  $V$ , the total instantaneous power generated,  $\Omega$ , is established. This theory was developed by Howe (1980, 1989) as a generalization of previous work done by Powell (1964), which provides a relationship between the vortex shedding and sound generation. Many authors used Howe's Theorem to describe and simulate the flow-sound interaction mechanism which generates acoustic resonances for a variety of flow situations such as Helmholtz resonators, closed side-branches, bluff bodies exposed to cross flow in ducts, and orifice plates in ducts (e.g., Nelson et al., 1983; Stoneman et al., 1988; Hourigan et al., 1990; Mohany and Ziada, 2009; Nakiboglu et al.,

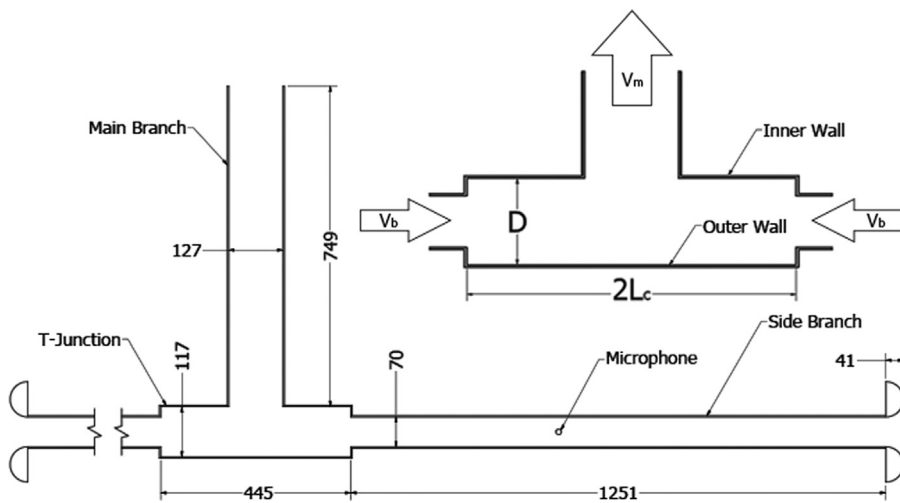


Fig. 1. Plan view of T-junction apparatus (all dimensions are in mm).

2011; Peugot and Frendi, 2013). For a more complete review, the reader is referred to the recent articles by Tonon et al. (2011) and Ziada and Lafon (2014).

## 2. Experimental apparatus and methods of analysis

### 2.1. Experimental apparatus

The present work was motivated by a vibration problem of a high-pressure steam pipe in a power plant. This problem has been investigated by Ziada et al. (2007, 2009), who showed that flow separation at the inlets of the T-junction shown in Fig. 1 is the source of acoustic excitation. Since long diffusers with small expansion angle are rather expensive to implement in high-pressure piping systems, pipeline suppliers often use short diffusers with large expansion angle, similar to the one which produced the vibration problems being investigated in this work. The previous investigations therefore focused on means of alleviating the acoustic resonance for pipes with large angle diffusers by either avoiding the flow range of resonance or implementing geometry changes in the piping system, such as detuning the branches by making them of different lengths or introducing asymmetry in the geometry of the T-junction expansion section (Ziada et al., 2007, 2009). The objective of the present study is to explore the details of the flow–sound interaction mechanism by means of particle imaging velocimetry (PIV) technique. In order to achieve this objective, the present experiments use ducts with rectangular, rather than cylindrical, cross-sections to simplify the flow field and treat it as two dimensional. In addition, the 45° expansion pieces at the inlets of the T-junction are replaced by sudden expansions of the duct's cross-section.

The T-junction test set-up is shown in Fig. 1. Typical geometries of T-junctions in industrial applications have an outlet pipe area approximately equal to the sum of the inlet pipe areas and thereby maintain approximately constant flow velocity in all pipes. This condition is achieved by means of the aforementioned expansion at the inlet of the T-junction as illustrated in Fig. 1. The requirement of approximately constant flow velocity, along with the availability of commercial rectangular tubing, constrained the choice of the cross sectional dimensions of the present test facility. In addition, the maximum blower capacity determined the maximum flow velocity in the selected ducts and therefore the length of the branches was selected to be sufficiently long to ensure the production of sustained resonance within the available blower capacity. Thus, the test facility consists of two co-axial (side) branches orthogonally positioned to a single main-branch while air is employed as the working fluid. The flow travels through the side-branches toward the T-junction where it merges and exits through the main branch. The entire test set-up is manufactured using rectangular tubing with a uniform depth, i.e., the height of the flow cross-section of all branches is maintained constant at 70 mm (2.75 in.). As well, the set-up is symmetric about the center plane of the main-branch. The side and main-branches are made of prefabricated 3.2 mm (1/8 in.) aluminum rectangular tubing. While the cross-section of the side-branches is 70 mm wide and its length is 1251 mm, the main-branch has a width of 127 mm (5 in.) and a length of 749 mm. The T-junction is made with 11.9 mm (15/32 in.) acrylic sheets to allow for sufficient optical access while maintaining stability. The region in the T-junction connecting the two side-branches (the transition section) has a length of  $2L_c = 445$  mm and a width of  $D = 117$  mm, creating a T-junction ratio of  $2L_c/D = 3.8$ .

To allow smooth flow entrance and diminish unwanted noise, flow turbulence and pressure drop, a bell mouth is placed at the inlet of each side-branch. Additionally, a diffuser is situated downstream of the main-branch to improve pressure recovery and reduce the overall pressure drop over the whole duct system. The diffuser is made of plywood and has a length of 1219 mm and an included angle of 7.1°. To isolate the test section from the blower vibration, a flexible hose is used to connect the diffuser exit to the suction side of the blower. Also revealed in Fig. 1, a hole drilled in the side-branch 743 mm from the center plane of the T-junction serves as a mounting point for a pitot tube and a flush mount microphone, used to measure the mean flow velocity and pressure pulsation, respectively.

### 2.2. Acoustic measurement setup

The pitot tube was utilized to calibrate the mean flow velocity in the side-branch with the frequency of the blower speed controller. The pressure difference in the pitot tube was determined using a Validyne DP15-36 pressure transducer in conjunction with a Validyne CD23 signal conditioner and a four channel National Instruments 9215 data acquisition device. The pressure transducer calibration was performed using a Crystal Engineering IS-33 pressure calibrator with a Ralston DPPV air pump. Applying a linear fit between the flow velocity in the side-branch,  $V_s$ , and the frequency of the blower speed controller,  $f_b$ , resulted in the relation  $V_s = 0.99f_b$  with a correlation constant  $r = 0.9996$ . Using mass conservation of the T-junction, the flow velocity in the main-branch,  $V_m$ , could then be realized as  $V_m = 1.09f_b$ .

As reported by previous studies (Ziada et al., 2007, 2009), the dominant mode of the piping system is the first resonant acoustic mode of the side-branches. This mode consists of a standing wave formed along the length of the side-branches with pressure nodes found at the inlets and at the center of the T-junction. Subsequently, pressure antinodes are established at the midpoints between the center of the T-junction and the inlets of the branches, precisely where the microphone is situated. The microphone used is a G.R.A.S.  $\frac{1}{4}$  in. Type 40CP condenser microphone, which produces a linear response within 1 dB deviation for frequencies between 4 Hz and 70 kHz and a 3% maximum distortion at 170 dB. Furthermore, a G.R.A.S. Type 26AB Preamplifier, a G.R.A.S. Type 12AA Power Supply and a National Instruments 9233 data acquisition unit containing four 24 bit IEPE analog inputs were utilized to acquire the microphone signal. A Type 42AB Pistonphone was used

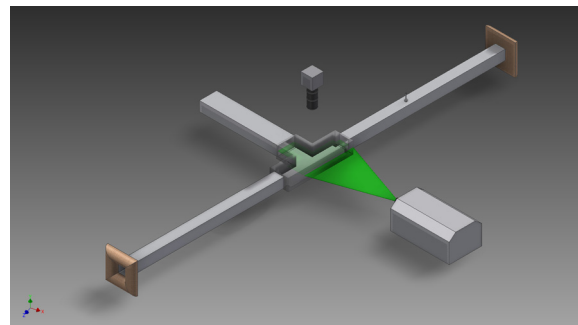


**Fig. 2.** Particle imaging velocimetry apparatus.

to calibrate the microphone equipment. The spectral analysis and averaging was completed at the time of acquisition using MATLAB. The test results from the aeroacoustic measurements will be presented here in terms of the dimensionless parameters; reduced velocity,  $V_r$ , and reduced pressure,  $P^*$ . These parameter are calculated as

$$V_r = \frac{V_m}{f_r L_c}, \quad (2)$$

$$P^* = \frac{P_{max}}{(1/2)\rho V_m^2}, \quad (3)$$

where  $V_m$  is the main pipe flow velocity,  $L_c$  is half the length of the T-junction,  $\rho$  is the density of the working fluid and  $P_{max}$  is the maximum RMS acoustic pressure at the frequency of the first resonant acoustic mode  $f_r$ .

### 2.3. Particle imaging velocimetry

The arrangement of the two-dimensional PIV system utilized in the current study to define the flow field in the T-junction can be reviewed in Fig. 2. To perform the measurements, a single Power View 4 MP CCD camera with a 12 bit dynamic range and a Nikon AF Nikkor 50 mm lens was used in conjunction with a 532 nm New Wave Solo 120XT pulsed Nd: YAG laser, capable of generating an output power of 120 mJ per pulse. A filter was situated on the end of the camera lens to allow only the bandwidth of light produced by the laser to pass through. A TSI LaserPulse Model 610035 synchronizer in combination with Insight 3G software was used to synchronize the camera and laser.

The flow was seeded with bis(2-ethylhexyl) sebacate via a Laskin aerosol generator, which creates a dispersion of particles with a mean diameter of 1  $\mu\text{m}$ . A sufficient quantity of seeding material was introduced to the flow such that each image contains vector validation rates in excess of 99.3%. The Stokes number based on the seed droplet properties and the maximum test flow velocity is less than 0.03, indicating a particle tracking error less than 1.2% (Melling, 1997).

At each of sixteen time instants within the acoustic cycle, uniformly spaced 22.5° apart, 150 image pairs were used to compute the velocity fields which were then averaged to determine 16 instantaneous velocity fields. An external trigger synchronized with the microphone signal provided a means of phase locking all 150 images with a known phase in the acoustic cycle. Aligning each point relative to the trigger was achieved using a small time delay available in the Insight 3G software.

Insight 3G was used to process each image separately via the Classical PIV algorithm. A standard 16 pixel square deformation grid was utilized which is computationally expensive but provides highly accurate analysis of flow fields containing high shear. The average vector field for each set of 150 images was computed using Tecplot and transferred to MATLAB for further processing. The vector field was computed for about 70% of the T-junction domain due to the limitations of the laser power. As discussed by Ziada et al. (2007, 2009), the flow fields of the T-junction's opposing sides are 180° out of phase mirror image and is displayed as such in the images to follow. The data and trends presented below have been validated against a series of images taken for the entire T-junction.

### 2.4. Finite element analysis

As discussed earlier, Howe's Theorem requires coupling of the flow field and the acoustic field to compute the acoustic power generation. As particle imaging velocimetry is used to define the flow field, which is the combined hydrodynamic and acoustic fields, another means is required to quantitatively express the acoustic field alone. In the present study, Finite Element Analysis (FEA) provided the acoustic mode shapes of the piping system and subsequently, the acoustic particle velocity. From previous studies (Ziada et al., 2009), it is known that a strong standing wave forms longitudinally throughout the length of the two side-branches as acoustic resonance occurs. The acoustic pressure field of this standing wave is the

product of two components, the spatial variation and the time variation as shown below

$$P_{ac}(x, y, z, t) = P_{FEA}(x, y, z) \cdot P_{mic}(t), \quad (4)$$

$$\text{where } P_{mic}(t) = P_{max} \sin 2\pi f_r t. \quad (5)$$

As the time variation,  $P_{mic}(t)$ , was measured by the microphone at the location of the maximum acoustic pressure, Abaqus software was used to conduct the FEA and determine the normalized spatial variation component,  $P_{FEA}(x, y, z)$ . By solving the Helmholtz equation for the entire piping system with no flow, the FEA determined the resonant frequency to be 119.6 Hz and produced the spatial pressure variation shown in Fig. 3. The acoustic particle velocity was found by solving Euler's equation of inviscid flow using the acoustic pressure distribution calculated from the finite element analysis

$$u_{ac} = -\frac{1}{\rho} \int \nabla P_{ac} dt, \quad (6)$$

$$u_{ac} = \frac{P_{max}}{\rho\omega} \nabla P_{FEA} \cos \omega t, \quad (7)$$

$$\text{where } \omega = 2\pi f_r. \quad (8)$$

The streamlines of the acoustic particle velocity in the T-junction can be seen overlying the pressure field in Fig. 3. As the acoustic particle velocity leads the acoustic pressure by 90°, these streamlines will reverse direction between 90° and 270° in the acoustic cycle. Furthermore, since the particle velocity is scaled by the gradient of the acoustic pressure field, the maximum acoustic particle velocity occurs near the center of the T-junction. This suggests this region has potential to provide significant contributions to the acoustic power generation.

### 3. Aeroacoustic response

T-junctions containing a sudden expansion (or transition region) are known to produce strong acoustic tones for a variety of flow velocities (Ziada et al., 2009). To determine the strength of said acoustic tones and the corresponding mean flow velocities at which they occur, a series of acoustic measurements were documented for a range of flow velocities. The flow velocity of the main-branch,  $V_m$ , was varied up to 68.1 m/s, which corresponds to the maximum capacity of the blower, in intervals of 1.09 m/s. At each flow velocity, fifty samples of the acoustic pressure signal were attained, with each sample comprised of 50 000 pressure measurements over one second. At the time of acquisition, individual frequency spectra were computed for individual samples of pressure signal and then averaged to obtain an averaged spectrum for the 50 samples acquired at each flow velocity. Scrutiny of the averaged frequency spectrum for each main-branch flow velocity, presented in the waterfall plot of Fig. 4(a), shows a constant 'lock-in' frequency of approximately 119 Hz for all of the acoustics tones generated. This lock-in frequency is in good agreement with the first resonant acoustic mode of the side-branches, which the FEA calculated to be 119.6 Hz.

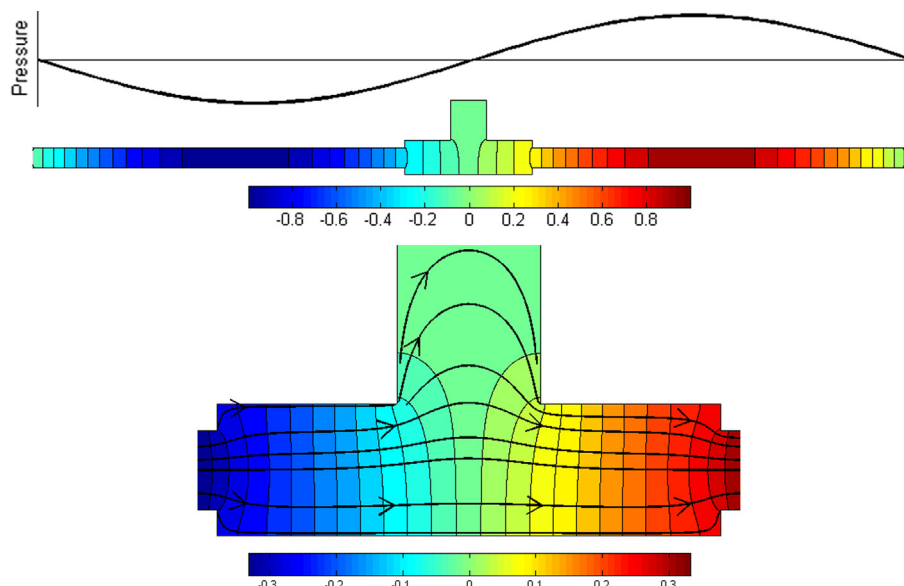


**Fig. 3.** Normalized acoustic pressure field,  $P_{FEA}$ , for the excited acoustic mode and a close up of the T-junction showing the acoustic particle velocity streamline.

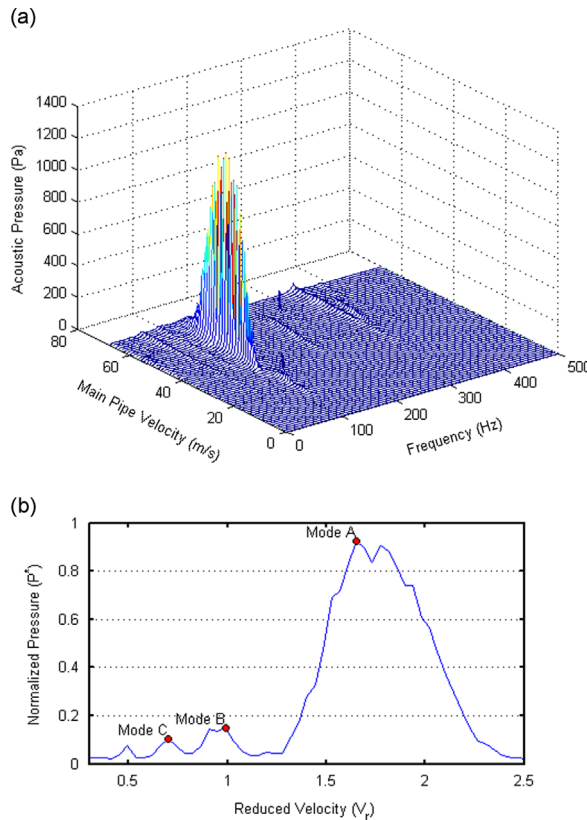


**Fig. 4.** Waterfall plot of frequency spectra of the aeroacoustic response of the system (a) and normalized acoustic pressure of the resonant acoustic mode as a function of reduced velocity in the main pipe (b).

The dimensionless amplitude response for the same data presented in Fig. 4(b) shows four distinct resonance peaks. It is not clear whether additional resonance peaks would have appeared at higher reduced velocities, as it was not possible to increase the flow velocity above that shown in Fig. 4(b). For this reason, the three largest peaks from right to left are denoted as shear layer modes A, B and C, respectively, rather than modes 1, 2 and 3. All three resonance peaks, or ranges, occur at the same frequency ( $\approx 119$  Hz), which corresponds to the first acoustic mode of the branches as shown in Fig. 3. This mode is excited at various velocity ranges by different hydrodynamic modes of the shear layer oscillation, with each shear layer mode corresponding to the formation of a certain number of instability wavelengths (or vortices) along the shear layer characteristic length ( $L_c$ ).

The PIV study presented below contains details of the unsteady flow field and acoustic power generation over the acoustic cycle for Mode A and Mode B. The flow velocity for the PIV measurements of Mode A is  $V_m = 43.7$  m/s ( $V_r = 1.65$ ) at which the self-excited amplitude reaches a maximum RMS acoustic pressure of 1079 Pa ( $P^* = 0.93$ ). PIV measurements of Mode B were performed at a main-branch flow velocity of 26.2 m/s ( $V_r = 0.99$ ), at which the RMS acoustic pressure reaches a value of 63 Pa ( $P^* = 0.15$ ). The ratio of maximum acoustic particle velocity to mean flow velocity in the main-branch ( $U_{ac}/V_m$ ) is 6.1% and 0.6% for Mode A and Mode B, respectively. PIV results were obtained for self-excited oscillation of Mode A, however as will be explained later, loudspeakers were used to enhance the much weaker oscillation of Mode B.

#### 4. Flow-sound interaction mechanism of Mode A ( $V_r = 1.65$ )

##### 4.1. Unsteady flow structure over the acoustic cycle

Fig. 5 reveals the unsteady flow field for Mode A at equally spaced phases in the acoustic cycle, corresponding to 17°, 107°, 197° and 287°. A single cycle of the acoustic pressure wave is presented at the top corner of each image, with a dot denoting the phase at which the image was taken. The images on the left show the velocity magnitude and particle streamlines, while the vorticity magnitude with contour lines of the  $d2$  parameter are shown on the right. The  $d2$  parameter, or the discriminant of the velocity gradient tensor, was developed by Vollmers (2001) and is used in the current study to identify the propagating coherent vortical structures, which have near-circular shapes, from the shear layers and boundary layers, which also contain strong vorticity. Even though the vorticity is high in the shear layers near the T-junction inlets, over the course of the acoustic cycle the flow pattern in these regions does not exhibit significant fluctuations. Consequently,

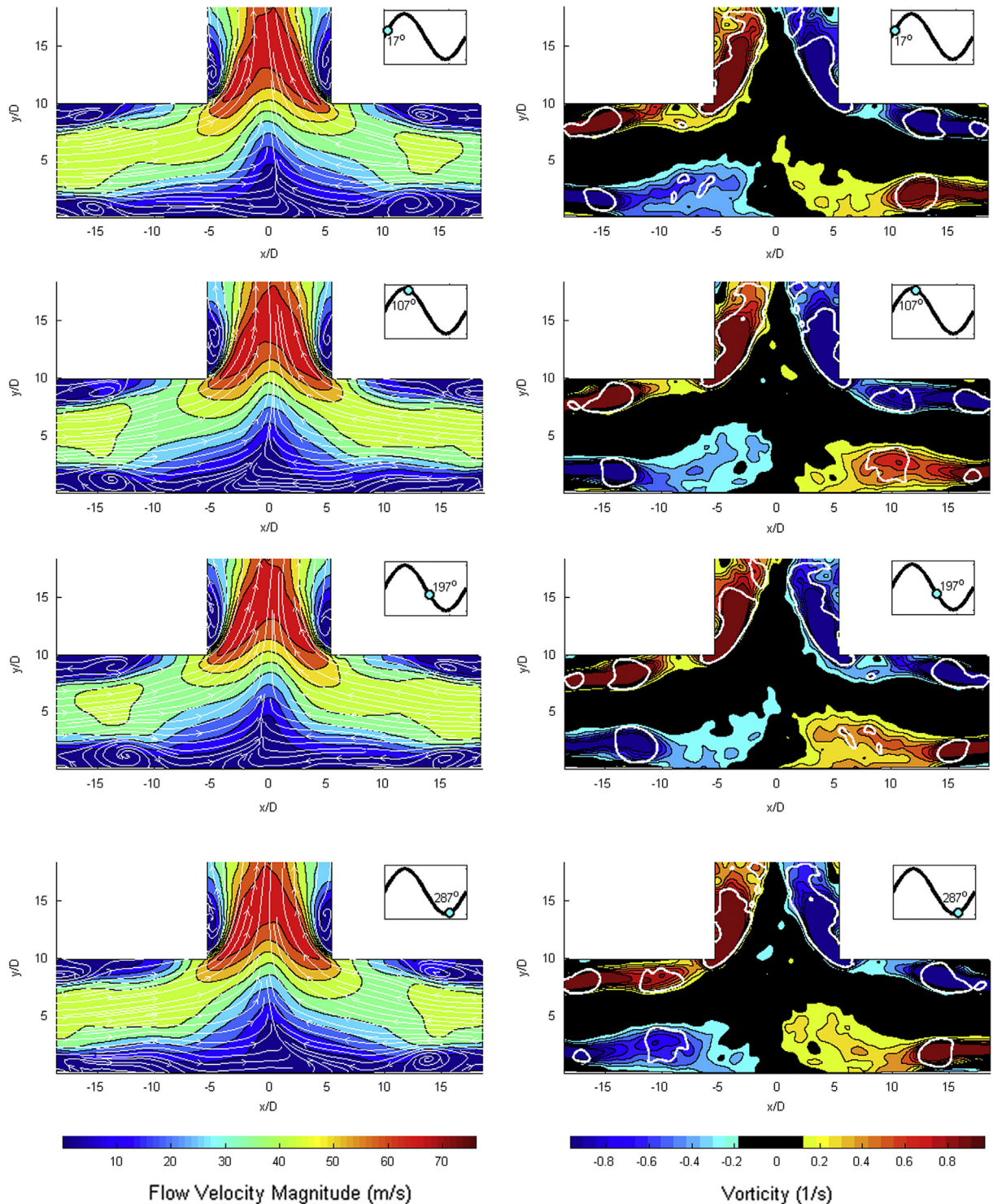


**Fig. 5.** Phase-averaged instantaneous flow velocity with streamlines (left) and vorticity with  $d_2$  parameter contours (right) for Mode A ( $V_r = 1.65$ ). The images correspond to the following phases of the acoustic cycle: 17°, 107°, 197° and 287°.

the power generated in one half of the acoustic cycle is counterbalanced by acoustic absorption in the succeeding half cycle as the acoustic particle velocity reverses direction. The sustained acoustic power contributions would appear to result from the coherent flow structures varying in vorticity as they propagate through the T-junction.

As the flow enters the T-junction and progresses along the transition region two shear layers on each side of the T-junction develop; a shear layer along the outer wall (the opposite wall from the T-junction exit) and a shear layer along the inner wall (next to the T-junction exit). When speaking only to the left side of the T-junction in Fig. 5, it is apparent that a vortex forms in each shear layer around  $270^\circ$ , which is precisely when the acoustic pressure is a maximum in the left branch and the acoustic particle velocity changes direction from left (against the flow) to right (with the flow). Over one full acoustic cycle, the vortex in each shear layer grows rapidly and propagates through the T-junction. Almost exactly one full acoustic cycle later, the same vortices begin to lose strength as a new vortex is formed and the cycle is repeated. Interestingly, the vortices on both the inner and outer shear layers form and propagate in phase with one another, suggesting that even though the shear layers are independent, they are synchronized by the acoustic pressure field. However, the vortex formed at the outer shear layer appears to propagate slightly faster. The right side of the T-junction is simply a  $180^\circ$  phase shifted mirror image of the left side since the maximum acoustic pressure will occur at  $90^\circ$  in the acoustic cycle as the acoustic particle velocity shifts from right to left.

As the vortical structures convect towards the center of the T-junction, the flow turns  $90^\circ$  towards the exit. The vortex along the inner wall is pushed against the wall, stretched, weakened and then ejected into the separation bubble located at the T-junction exit corner. On the other hand, the vortex along the outer wall moves away from the wall, its vorticity becomes distributed over a larger area and forms a large size vorticity blob that is “pumped” across the acoustic streamlines towards the exit of the T-junction. A close up of the weaker vorticity field at the center of the T-junction is shown in Fig. 6. Interestingly, although being less defined and weaker in strength, the vorticity blobs are seen to maintain their vorticity direction as they are transported across the T-junction and towards its exit. This feature will inevitably prove important as the acoustic power generation is discussed below. The progressive velocity contours on the left of Fig. 5 show the pulsing of the flow through the center of the T-junction as the vorticity blob passes. This pulsing flow action causes swinging of the centerline where the streamlines from each side-branch converge.

#### 4.2. Instantaneous acoustic power generation

Based on the assumption that the flow in the T-junction is basically two-dimensional, the PIV images obtained in the previous section contain the main features of the flow field. In other words, neglecting of the fluctuating component in the third dimension would have only minor effects on the flow-acoustic coupling mechanism. Therefore, the use of these flow images to compute the generation of instantaneous acoustic power by means of Howe's Theorem is adequate. Although this assumption does not hold near the sidewalls of the ducts and especially near the center of the T-junction, it is believed that it will have minor effects on the general behavior observed in this study. At the very least, the present results are expected to qualitatively describe the flow-sound interaction mechanism in the T-Junction. In fact, the final results of the spatial distribution of aeroacoustic sources in the T-junction will be seen to reflect a very orderly two-dimensional flow structure which lends support to the two-dimensionality assumption.

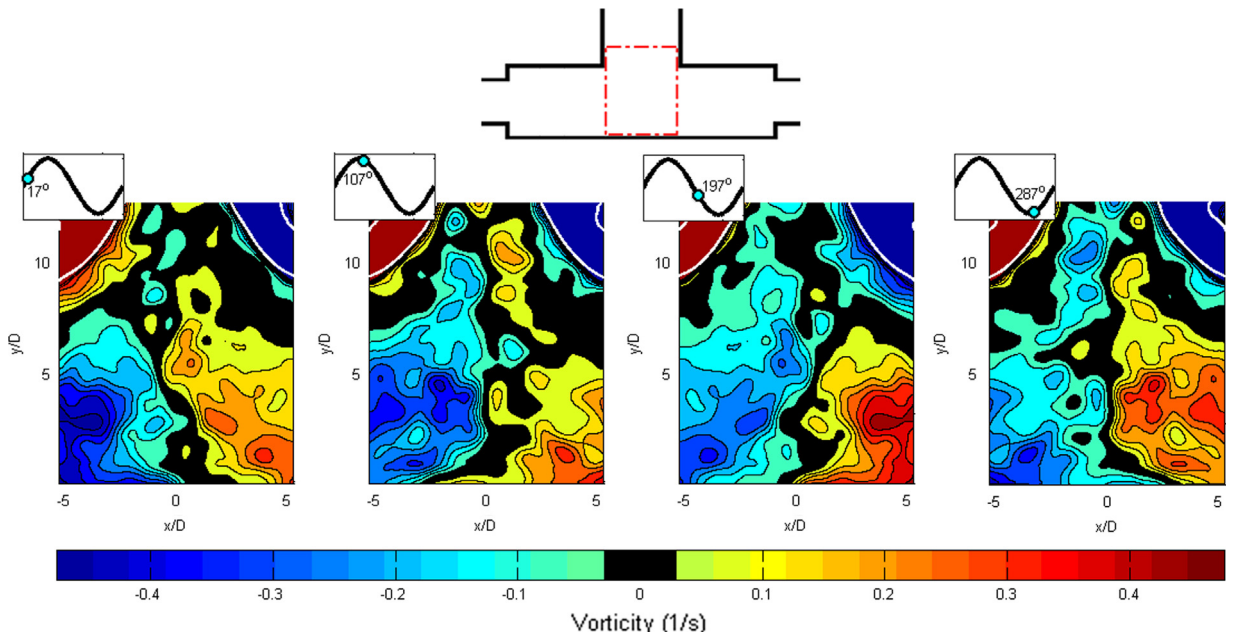


**Fig. 6.** Close up of phase-averaged instantaneous vorticity field at T-junction center for Mode A, with magnified vorticity scale ( $V_r = 1.65$ ).

In order to apply Howe's Theorem to compute the spatial distribution of acoustic energy generation, the hydrodynamic velocity field in the T-junction needs to be extracted from the measured velocity field presented in Fig. 5, which presents the combined hydrodynamic and acoustic field. This is achieved by subtracting the particle velocity field obtained from the finite element simulation, scaled by the microphone signal, from the total velocity field measured by the PIV system. Since the PIV measurements were phase-locked by the microphone signal, the phase of every PIV image within the acoustic cycle was well defined. Typical results of this process when the instantaneous acoustic particle velocity is near its maximum are illustrated in Fig. 7, where the total velocity and vorticity fields are given to the right and the hydrodynamic counterparts are shown to the left. The difference is seen to be small because the acoustic particle velocity is only 6.1% of the mean flow velocity.

Howe's Theorem for a two-dimensional flow field can also be written as

$$\Omega = -\rho \int \omega_z |v| |u_{ac}| \sin \phi dV. \quad (9)$$

In this equation,  $v$  and  $\omega_z$  are the hydrodynamic flow velocity and vorticity, as illustrated in Fig. 7, and  $\phi$  is the angle between the flow velocity,  $v$ , and the acoustic particle velocity,  $u_{ac}$ , vectors. Along the entrance region of the T-junction,  $\sin \phi$  remains small almost everywhere as there is minimal deviation between the streamlines of the particle velocity and the mean flow field. However, the propagation of the swirling structures through this region creates a normal component between said vectors, effectively establishing a basis for energy exchanges between the flow field and the acoustic field. The rotation of the vortices in both the inner and outer shear layers is such that the velocity field ahead of the vortex has a component away from the center axis of the inlet ducts and behind the vortex has a component toward the center axis. Consequently, each vortex creates an aeroacoustic source with sound generation on one side and absorption on the other. The orientation of the source and sink in this structure is such that the acoustic particle velocity streamlines will be directed from sink to source as they pass through the vortex. This phenomenon can be observed in the phase locked instantaneous

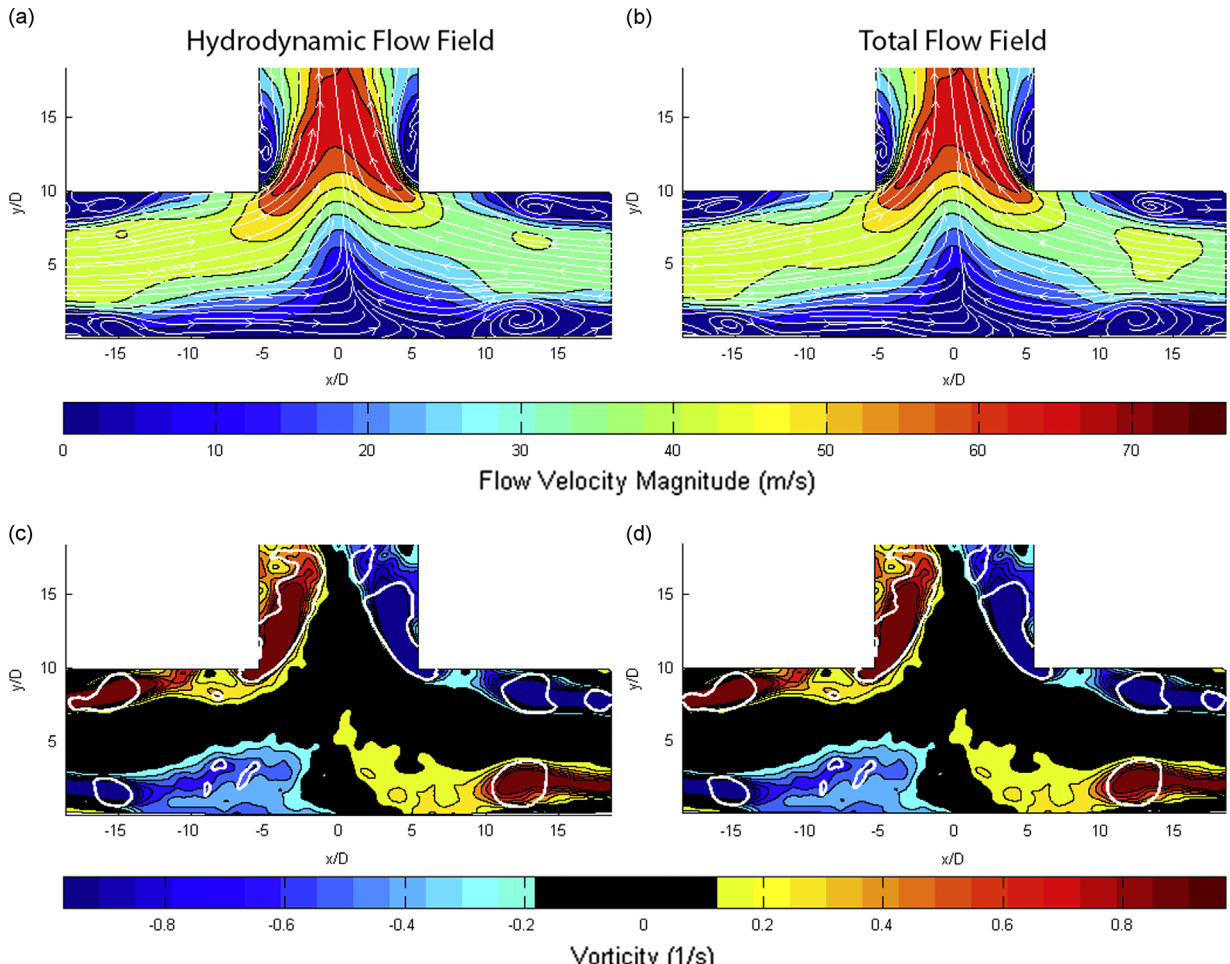


**Fig. 7.** Comparison of the hydrodynamic (left) and the total (right) flow fields for Mode A ( $V_r = 1.65$ ) at phase  $17^\circ$  in the acoustic cycle, showing both the phase-averaged instantaneous flow velocity with streamlines (top) and vorticity with  $d2$  parameter contours (bottom).

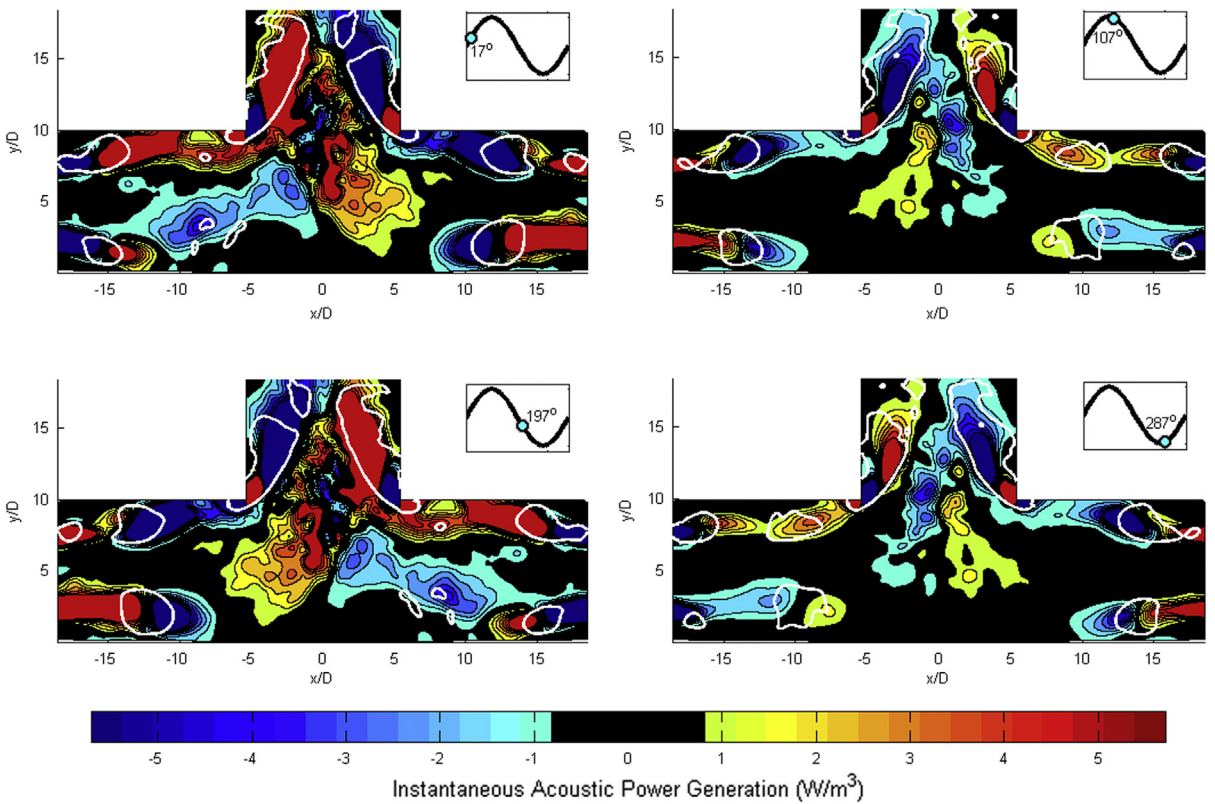


**Fig. 8.** Phase-averaged instantaneous acoustic power generation with  $d2$  parameter contours for Mode A ( $V_r = 1.65$ ).

acoustic power generation displayed in Fig. 8, as the vortices are outlined using the same  $d2$  parameter used to define the flow field earlier.

Furthermore, as the vorticity blobs, formed by the vortices along the outer wall, convect through the center of the T-junction, the streamlines of the velocity field become increasingly normal to the direction of acoustic particle velocity streamlines. As a result, the effect of the vorticity on the flow becomes less pronounced causing the combined source-sink structure generated by the flow-acoustic interaction to develop into a single source or sink, driven by the cross-product between the orthogonal components of the acoustic particle velocity and flow velocity. As the vorticity blob traverses across the center of the T-junction and out through its exit, the acoustic particle velocity is always opposing the direction at which the vorticity blob developed from, resulting in an acoustic power source. This acoustic power source increases in strength as it approaches the exit of the T-junction as a result of the increasing flow velocity, as well as the growing orthogonality between the acoustic particle velocity and the flow velocity.

#### 4.3. Net acoustic power transfer per cycle

As illustrated in Fig. 8, the instantaneous spatial distribution of acoustic power generation/absorption varies with time. To obtain the spatial distribution of net acoustic power transfer per cycle, the instantaneous images for one acoustic cycle are summed up, which results in the contour plot of Fig. 9(a), showing the locations of the aeroacoustic sources and sinks. The alternating pattern of the acoustic power along the length of the entrance region (e.g.,  $5 < |x/D| < 20$ ) is clearly shown in this figure. These acoustic sources and sinks grow in strength and diameter as they convect towards the center of the T-junction, which is a direct reflection of the growing nature of the vortices in this region.

From Fig. 9(a), the power generated at each  $x$  location can be integrated over the width of the duct, i.e., over various values of  $y/D$  for constant  $x$ -position. This spanwise acoustic power generation (APG) is depicted by the solid red curve in Fig. 9(b) along the streamwise location inside the T-junction. The total cumulative power produced by the flow from the entrance on the left to the center of the T-junction can be obtained by integrating the spanwise APG along the  $x$  direction from  $x/D = -20$  to 0, and is given by the dotted blue curve in Fig. 9(b). Even with the increasing size of the sources and sinks, the alternating direction of energy flow resulted in the total power generated along the entrance region to be minimalistic, as shown by the cumulative power near  $x/D = -5$ . Subsequently, the power produced in the center of the T-junction is what produces the difference in the overall acoustic power emitted by the flow. Remarkably, even though there are dominant flow structures throughout the T-junction, the remnants of the weak dispersed vortices passing through the center of the

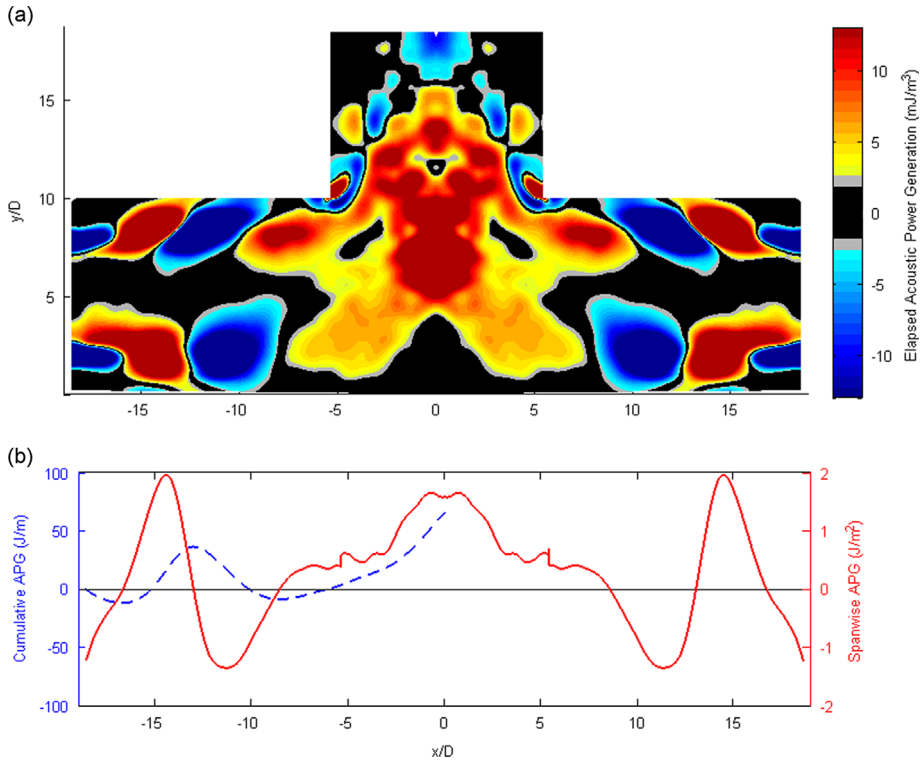


**Fig. 9.** Top figure shows distribution of aeroacoustic sources (red color) and sinks (blue color) in the T-junction for Mode A. Lower figure shows spanwise power generation (solid red curve) and cumulative power from the left entrance to the center of the T-junction (dotted blue curve) for Mode A ( $V_r = 1.65$ ). (For interpretation of the references to color in this figure legend, the reader is referred to the web version of this article.)

T-junction discussed earlier is what powers the acoustic mode of the piping system. This provides some insight into the mechanism which explains why vorticity shedding along the outer wall of the transition region is required to produce most of the net acoustic power driving the acoustic resonance, as proposed by Ziada et al. (2009).

## 5. Flow–sound interaction mechanism of Mode B ( $V_r = 0.99$ )

### 5.1. Unsteady flow structure over the acoustic cycle

When the acoustic resonance was excited by Mode B of the shear layer oscillation near  $V_r = 0.99$ , the resulting sound pressure was rather weak as illustrated in Fig. 4. In fact, the normalized particle velocity under the self-excitation conditions amounted to only  $(U_{ac}/V_m) = 0.6\%$ . The PIV images produced under this condition of self-excitation were unclear and included a large degree of variability. For this reason, two loudspeakers, one placed near each branch inlet, were used to enhance the resonance at flow conditions compatible with Mode B excitation, i.e. at  $V_r = 0.99$ . This excitation increased the normalized acoustic particle velocity ( $U_{ac}/V_m$ ) to 6.2%, which is close to the self-excited resonance by shear layer Mode A. The flow field associated with shear layer Mode B is similar to that of Mode A in many respects. Both the velocity field and vorticity field for Mode B are shown in Fig. 10. As in Mode A, there are shear layers present on both the inner and outer walls of the entrance region to the T-junction. Additionally, both the shear layers on the inner wall and outer wall produce one vortex per cycle which grows, propagates, and dissipates in phase with one another. Since the geometry and the acoustic mode has not changed from the previous case, the mean flow and the acoustic particle streamlines are also similar to Mode A oscillation, but have only a fraction of the corresponding velocity magnitudes. As Mode B oscillation occurs at a lower flow velocity, the vortices do not propagate as rapidly as in Mode A oscillation. Subsequently, it takes one more full acoustic cycle than in Mode A for the vortices to propagate through the T-junction. The vortices also grow over two acoustic cycles before they begin to dissipate, instead of one cycle as in the case of Mode A. However, similar to Mode A oscillation pattern, the vortices along the inner wall are stretched when reaching the sharp corner at the T-junction exit and are then ejected into the separation bubble behind the sharp corner. The difference in the convection velocities of the vortical structures along the inner and outer walls of the T-junction is slightly larger than observed in Mode A, as the outer shear layer convects faster.

The contour lines showing the  $d_2$  parameter on the vorticity plots in Fig. 10 highlight two circular stationary spinning structures in the center of the T-junction along the outer wall. The vortices propagating along the outer wall appear to

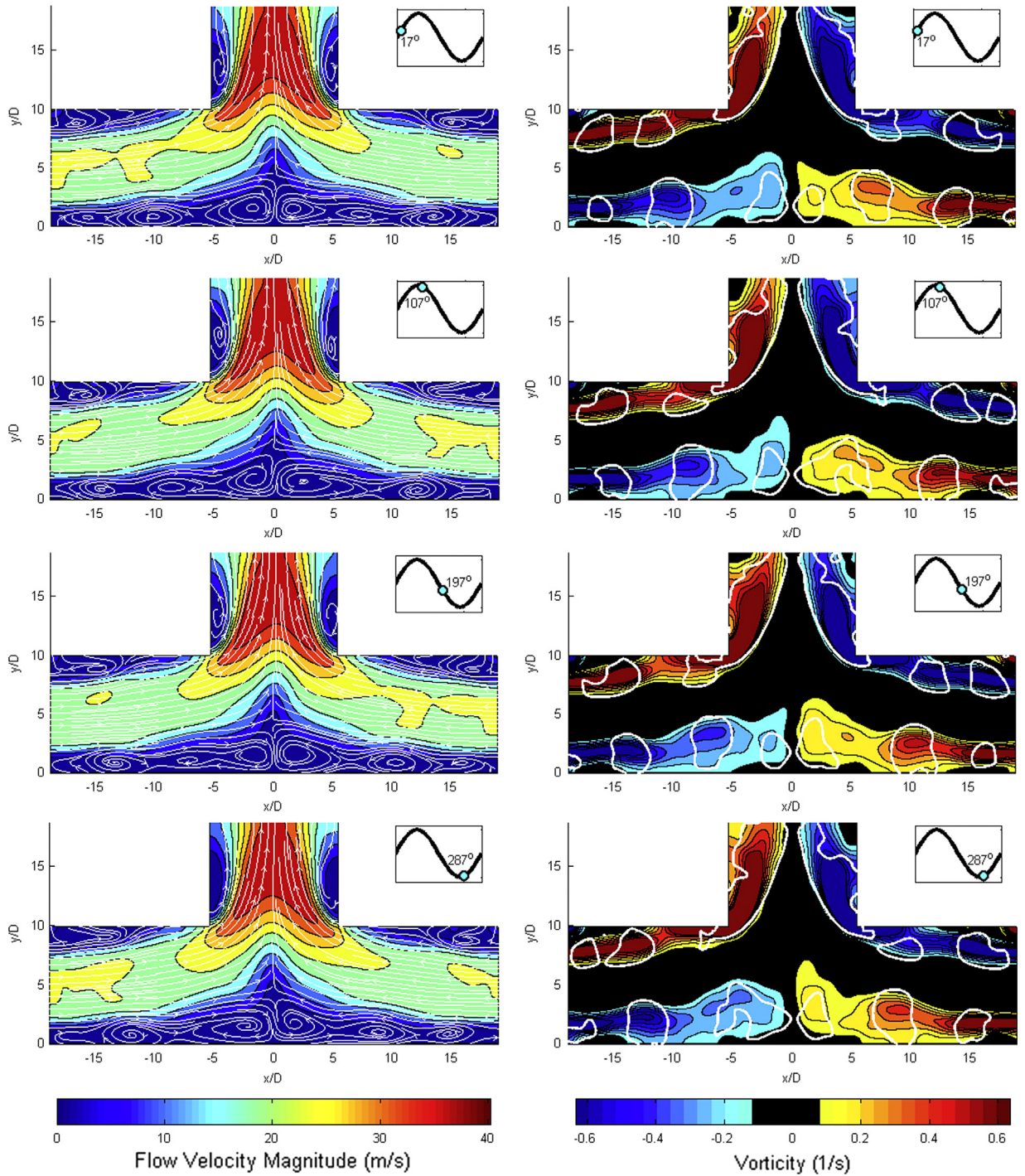


**Fig. 10.** Phase-averaged instantaneous flow velocity with streamlines (left) and vorticity with  $d_2$  parameter contours (right) for Mode B ( $V_r = 0.99$ ). The images correspond to the following phases of the acoustic cycle: 17°, 107°, 197° and 287°.

merge with these structures as they reach the center of the T-junction. However, a more detailed observation of the vorticity field in this region, shown in Fig. 11, indicates that much of the vorticity blob along the outer wall convects right over the stationary structure. In any case, similar to Mode A oscillation, the vorticity blobs are redirected toward the exit of the T-junction. As seen in the velocity fields present in Fig. 10, there is weak swinging motion of the centerline where the flows from each side-branch converge, however the amplitude of this swing oscillations is much smaller than that observed for Mode A. This can be attributed to the weaker pulsing of the flow field since the vortices are traveling at a slower rate.

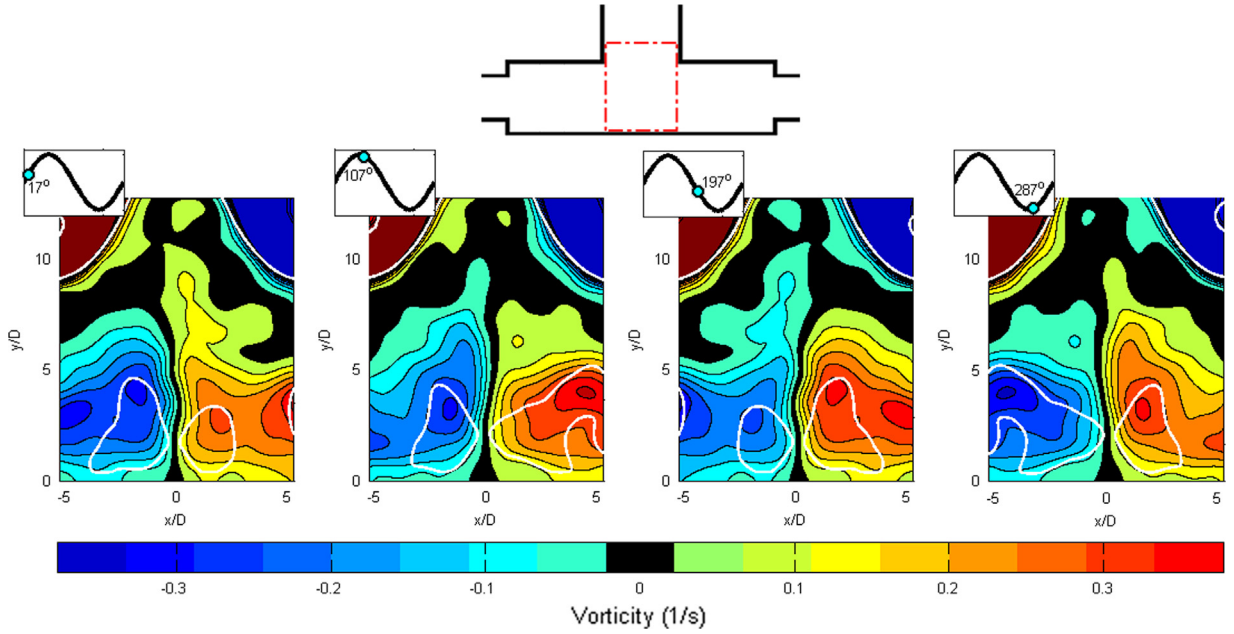


**Fig. 11.** Close up of phase-averaged instantaneous vorticity field at T-junction center for Mode B, with magnified vorticity scale ( $V_r = 0.99$ ).

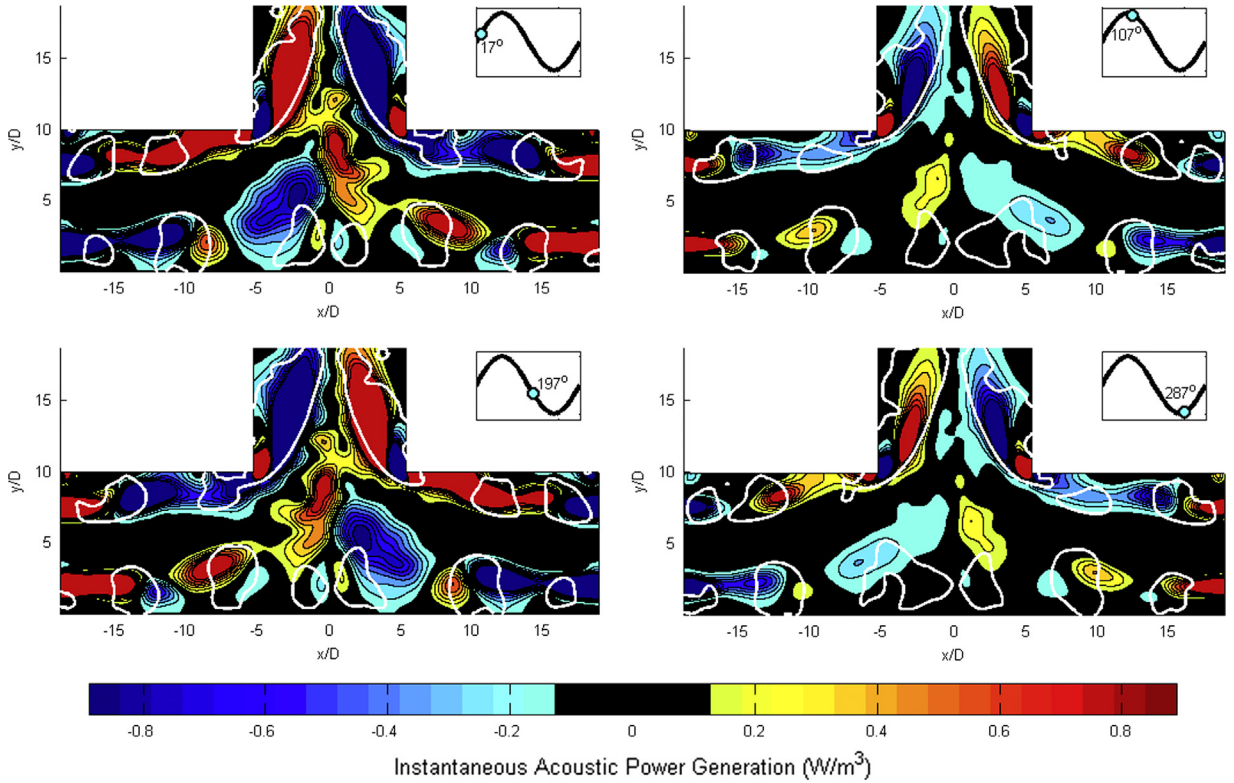


**Fig. 12.** Phase-averaged instantaneous acoustic power generation with  $d_2$  parameter contours for Mode B ( $V_r = 0.99$ ).

## 5.2. Instantaneous acoustic power generation

As in the previous case, the acoustic particle velocity vectors were subtracted from the total velocity field shown in Fig. 10 to obtain the hydrodynamic velocity and vorticity fields and apply Howe's Theorem. The resulting temporal acoustic power distribution is presented in Fig. 12 together with the locations of the coherent vortical structures as specified by the  $d_2$

parameter. Similar to Mode A oscillation, the acoustic power generation takes a combined source-sink structure around the vortices along the entrance region, with the acoustic particle velocity streamlines traveling from sink to source as they pass through the vortex. However, the point at which the power generation develops into a single source or sink around the vortex is located closer to the center of the T-junction, relative to Mode A. Because of the increased number of vortices than observed in Mode A, the acoustic power generation appears to have more concentrated nodes along the length of the outer wall. Comparison of Figs. 11 and 12 indicates that the vorticity blobs in Fig. 11 are closer to the outer wall than the sound sources in Fig. 12, which are more displaced towards the T-junction exit. This difference is due to the increasing velocity component orthogonal to the acoustic streamlines away from the outer wall. Since the vorticity blobs exit the T-junction at exactly one full acoustic cycle later than Mode A, the flow–sound interaction at this location still results in an acoustic source.

### 5.3. Net acoustic power transfer per cycle

The spatial distribution of the local acoustic energy transfer between the flow and the acoustic resonant mode over an acoustic cycle is shown in Fig. 13(a). Comparison of this figure with Fig. 9(a) for shear layer Mode A elucidates the effect of the slower convection rates of the vortical structures by shear layer Mode B. The presence of an additional vortical structure at any point in the acoustic period results in the creation of an additional sink and source along the path of each vortex and therefore a larger number of acoustic sources/sinks are generated in Mode B than in Mode A. The sources and sinks still increase in magnitude as they near the center of the T-junction, indicative of their growing strength.

The local spanwise APG is shown by the solid red curve in Fig. 13(b) and the integration of this curve yields the cumulative power generated along the  $x$  direction starting from  $x/D = -20$  to 0, which is given by the dotted blue curve in the same figure. Similar to the case of Mode A, the cumulative power generated by the shear layer oscillation at Mode B amounts to almost zero over the branch inlets (i.e., from  $x = -20$  to  $-5$ ). Here also, the sound power generated at the center of the T-junction seems to hold the balance whether the total accumulated power will be positive or negative.

Comparing Figs. 9(a) and 13(a) again, two main differences between shear layer Modes A and B become apparent. First, the strength of the aeroacoustic sources and sinks of shear layer Mode B is about an order of magnitude weaker than those resulting from Mode A. This difference seems reasonable because the resonance caused by Mode A is much stronger than that caused by Mode B, as has already been illustrated in Fig. 4. This difference also agrees well with the measurements of shear layer excitation sources for deep and shallow cavities which showed that higher order shear layer modes have much

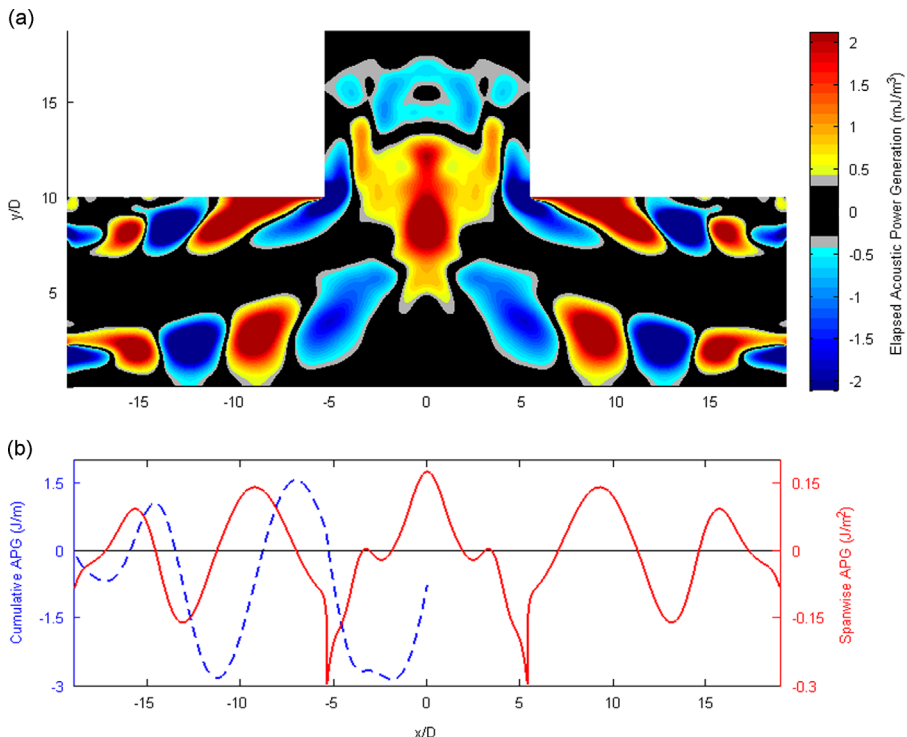


**Fig. 13.** Top figure shows distribution of aeroacoustic sources (red color) and sinks (blue color) in the T-junction for Mode B. Lower figure shows spanwise power generation (solid red curve) and cumulative power from the left entrance to the center of the T-junction (dotted blue curve) for Mode B ( $V_r = 0.99$ ). (For interpretation of the references to color in this figure legend, the reader is referred to the web version of this article.)

weaker excitation sources than those generated by the lower shear layer modes (Graf and Ziada, 2010; Mohamed et al., 2011; Nakiboglu et al., 2011). The second difference is that the accumulated sound power for Mode B oscillation is a small negative value, whereas the power computed for Mode A was positive. It should be pointed out that the present results for Mode B were obtained by applying external sound excitation and thereby increasing the pulsation amplitude artificially. It is well established that the excitation sources of shear layers become weaker at large amplitude acoustic pulsation, and especially for sources associated with higher shear layer modes. For example, Mohamed et al. (2011) demonstrated that the second shear layer mode of a shallow cavity becomes negative at an excitation level of  $(U_{ac}/V_m) \approx 4\%$ . In the present case, the excitation level was even higher due to external excitation  $(U_{ac}/V_m) = 6.2\%$ , and therefore the total accumulated power is negative, indicating that some of power provided by the loudspeakers is absorbed by the flow oscillations in the T-junction. The transformation of acoustic sources into sinks at large amplitude acoustic pulsation is referred to in the literature as the vortex dampening and results in an overall exchange of energy from the acoustic field to the flow field.

As three periods of the acoustic cycle are required for the vortex to convect through the T-junction in Mode B and two periods are required in Mode A, it is possible that there exists another shear layer mode for which the formed vortical structures require only one cycle to traverse through the T-junction. If this is true, then this shear layer mode would contain only one vortical structure in the entrance region and would occur at a reduced velocity which is higher than the range of blower capacity.

## 6. Conclusion

The present study revealed a series of shear layer modes exciting the acoustic mode of the branches with a pressure node at the T-junction. The unsteady flow fields associated with two modes of the shear layer oscillation were detailed by means of phase-locked PIV measurements. Finite element analysis was also performed on the piping geometry to determine the details of the resonant acoustic mode. Combining the unsteady flow field and acoustic field with the aid of Howe's Theorem provided new insights into the flow–sound interaction mechanism in the T-junction and resulting energy transfer patterns between said fields. At the entrance of the T-junction, where a sudden flow expansion exists, a rapid formation and growth of vortical structures in the separated shear layers is observed. In Mode A, which occurs at a higher reduced velocity near 1.6, the vortical structures grew over one cycle before beginning to disperse into a larger vorticity blob near the T-junction center, while in Mode B, which occurs near reduced velocity of 1.0, the vortical structures continued to grow over two cycles. As these vortical structures grow in the shear layer along the entrance region, an acoustic source is formed on one side of the structure while an acoustic sink is formed on the opposing side. The orientation of the source and sink around these vortical structures is such that the acoustic particle streamlines are directed from sink to source. Since the acoustic particle velocity is able to oscillate while the vortex translates through the entrance region, the spatial distribution of net acoustic power generation shows an alternating acoustic power structure in this region, which cumulatively results in minimal net energy exchange between the flow and sound field. However, when the vorticity blob is diverted transversely towards the exit of the T-junction, the entire structure becomes a single source or sink. In both shear layer modes, the vorticity blob formed at the outer wall leaves the T-junction generating a strong acoustic source, but after completing three full acoustic cycles in Mode B and only two in Mode A.

## References

- Bruggeman, J.C., Hirschberg, A., van Dongen, M.E.H., Wijnands, A.P.J., Gorter, J., 1989. Flow induced pulsations in gas transport systems: analysis of the influence of closed side branches. *Journal of Fluids Engineering* 111, 484–491.
- Bruggeman, J.C., Hirschberg, A., van Dongen, M.E.H., Wijnands, A.P.J., Gorter, J., 1991. Self-sustained aero-acoustic pulsations in gas transport systems: experimental study of the influence of closed side branches. *Journal of Sound and Vibration* 150, 371–393.
- Coffman, J.T., Bernstein, M.D., 1980. Failure of safety valves due to flow induced vibration. *Journal of Pressure Vessel Technology* 102, 112–118.
- Dequand, S., Hulshoff, S.J., Hirschberg, A., 2003. Self-sustained oscillations in a closed side-branch system. *Journal of Sound and Vibration* 265 (2), 359–386.
- Fagerlund, A., Catron, F., Karzub, D., Martin, T., 2005. Identification and prediction of piping system noise. *Journal of the Acoustical Society of America* 118 (3), 1869.
- Graf, H.R., Ziada, S., 2010. Excitation source of a side-branch shear layer. *Journal of Sound and Vibration* 329 (14), 2825–2842.
- Hirschberg, A., Bruggeman, J.C., Wijnands, A.P.J., Smits, N., 1989. The whistler nozzle and horn as aero-acoustic sound sources in pipe systems. *Acta Acustica* 68 (2), 157–160.
- Hourigan, K., Welsh, M.C., Thompson, M.C., Stokes, A.N., 1990. Aerodynamic sources of acoustic resonance in a duct with baffles. *Journal of Fluids and Structures* 4, 345–370.
- Howe, M.S., 1980. The dissipation of sound at an edge. *Journal of Sound and Vibration* 70, 407–411.
- Howe, M.S., 1998. *Acoustics of Fluid-Structure Interactions*. Cambridge University Press, Cambridge.
- Karlsson, M., Åbom, M., 2010. Aeroacoustics of T-junctions—an experimental investigation. *Journal of Sound and Vibration* 329 (10), 1793–1808.
- Koo, G.H., Park, Y.S., 1998. Vibration reduction by using periodic supports in a piping system. *Journal of Sound and Vibration* 210 (1), 53–68.
- Melling, A., 1997. Tracer particles and seeding for particle image velocimetry. *Measurement Science and Technology* 8 (12), 1406.
- Mohamed, S., Graf, H.R., Ziada, S., 2011. Aeroacoustic source of a shallow cavity in a pipeline. In: Proceedings of ASME Pressure Vessels and Piping Conference, Volume 4: Fluid-Structure Interaction, Paper no. PVP2011-57437, pp. 269–276.
- Mohany, A., Ziada, S., 2009. Numerical simulation of the flow–sound interaction mechanisms of a single and two tandem cylinders in cross-flow. *Journal of Pressure Vessel Technology* 131, 031306.
- Nakiboglu, G., Belfroid, S., Golliard, J., Hirschberg, A., 2011. On the whistling corrugated pipes: effect of pipe length and flow profile. *Journal of Fluid Mechanics* 672, 78–108.
- Nelson, P.A., Halliwell, N.A., Doak, P.E., 1983. Fluid dynamic of a flow excited resonance. *Journal of Sound Vibration* 91, 375–402.
- Peugot, J.W., Frendi, A., 2013. Toward the understanding of flow-induced vibrations in a rocket-engine manifold. *Journal of Propulsion and Power* 29 (6), 1468–1477.

- Powell, A., 1964. Theory of vortex sound. *Journal of the Acoustical Society of America* 36 (1), 177–195.
- Rockwell, D., Naudascher, E., 1978. Review-self-sustaining oscillations of flow past cavities. *Journal of Fluids Engineering* 100, 152–165.
- Stoneman, S.A.T., Hourigan, K., Stokes, A.N., Welsh, M.C., 1988. Resonant sound caused by flow past two plates in tandem in a duct. *Journal of Fluid Mechanics* 192, 455–484.
- Tonon, D., Hirschberg, A., Goliard, J., Ziada, S., 2011. Aeroacoustics of pipe systems with closed branches. *International Journal of Aeroacoustics* 10 (2-3), 201–276.
- Vollmers, H., 2001. Detection of vortices and quantitative evaluation of their main parameters from experimental velocity data. *Measurement Science and Technology* 12 (8), 1199–1207.
- van Lier, L., Dequand, S., Hirschberg, A., Corts, J., 2001. Aeroacoustics of diffusers: an experimental study of typical industrial diffusers at Reynolds numbers of  $O(10^5)$ . *Journal Acoustic Society of America* 109, 108–115.
- Ziada, S., 1994. A flow visualization study of flow-acoustic coupling at the mouth of a resonant side-branch. *Journal of Fluids and Structures* 8 (4), 391–416.
- Ziada, S., 2010. Flow-excited acoustic resonance in industry. *Journal of Pressure Vessel Technology* 132 (1), 015001.
- Ziada, S., Bühlmann, E.T., 1992. Self-excited resonances of two side-branches in close proximity. *Journal of Fluids and Structures* 6 (5), 583–601.
- Ziada, S., Lafon, F., 2014. Flow-excited acoustic resonance: excitation mechanism, design guidelines and counter-measures. *Applied Mechanics Review* 66 (1), 010802.
- Ziada, S., McLaren, K.W., Li, Y., 2009. Flow-acoustic coupling in T-junctions: effect of T-junction geometry. *Journal of Pressure Vessel Technology* 131 (4), 041302.
- Ziada, S., Scott, A., Arthurs, D., 2007. Acoustic excitation by flow in T-junctions. *Journal of Pressure Vessel Technology* 129 (1), 14–20.